ELASTOINERTIAL TURBULENCE AND CONNECTIONS TO LINEAR MECHANISMS

Ashwin Shekar
Department of Chemical and Biological Engineering
University of Wisconsin-Madison
Madison WI 53706,USA
shekar2@wisc.edu

Ryan M. McMullen
Graduate Aerospace Laboratories
California Institute of Technology
Pasadena CA 91125, USA
mcmullen@caltech.edu

Beverley J. McKeon
Graduate Aerospace Laboratories
California Institute of Technology
Pasadena CA 91125, USA
mckeon@caltech.edu

Michael D. Graham
Department of Chemical and Biological Engineering
University of Wisconsin-Madison
Madison WI 53706,USA
mdgraham@wisc.edu

ABSTRACT

One of the most puzzling and dramatic phenomena in non-Newtonian flow is the substantial reduction of turbulent energy dissipation (drag) that occurs when a small amount of a long-chain polymer is added to a liquid. If the Reynolds number is sufficiently low, a turbulent channel flow will laminarize as polymer concentration increases, but then become turbulent again at higher concentration. Direct simulations of flow in the latter "elastoinertial turbulence" (EIT) regime indicate the presence of localized polymer stretch fluctuations. These observations, along with linear stability and resolvent analyses, show that the turbulent fluctuations resemble Tollmien-Schlichting (TS) modes. Although these are found in Newtonian flows, they do not play a role in fully-developed Newtonian turbulence. In the polymeric case, however, polymer stresses suppress the normal turbulent structures while amplifying the TS modes. Finally, we present results on the existence of a new nonlinear self-sustaining state which we term the lower branch attractor (LBA), which coexists in parameter space with EIT but has very small amplitude. The structure of this flow very closely resembles that of the linear TS mode. A tentative bifurcation scenario describing our observations is presented.

RESULTS

For polymer solutions under some flow conditions, transition to turbulence occurs via the usual bypass transition as Reynolds number *Re* increases. With further increase in *Re*, onset of drag reduction occurs and the flow eventually approaches the so-called maximum drag reduction (MDR) asymptote, an experimental upper bound on the degree of drag reduction.

Under other conditions, however, flow transitions directly from laminar flow into the MDR regime and can do so at a Reynolds number where the flow would remain laminar if Newtonian. This phenomenon is known as "early turbulence" (Forame *et al.* (1972); Choueiri *et al.* (2018)). Recent experiments and simulations (Samanta *et al.* (2013); Sid *et al.* (2018)) suggest that turbulence in this regime has structure very different from Newtonian, denoting it as "elastoinertial turbulence" (EIT). Choueiri *et al.* (2018) experimentally observed that at very low (i.e. transitional) Reynolds numbers and increasing polymer concentration, turbulence is first suppressed, leading to relaminarization, and then reinitiated with an EIT structure and a level of drag corresponding to MDR. This result indicates that there are actually two distinct types of turbulence in polymer solutions, one that is suppressed by viscoelasticity, and one that is promoted.

The present work extends Shekar *et al.* (2019), reporting computations and analysis for plane channel flow of a FENE-P fluid that elucidate the mechanisms underlying EIT. We show that EIT at low *Re* has highly localized polymer stress fluctuations. Surprisingly, these strongly resemble linear Tollmien-Schlichting modes as well as the most strongly amplified perturbations from the laminar state. Furthermore, the kinematics of self-sustained nonlinear TS waves generate sheetlike structures in the stress field similar to those observed in EIT. Lastly, we establish the existence of a new nonlinear self-sustaining attractor whose amplitude is very small relative to EIT and whose bulk structure very closely resembles the linear TS mode.

Formulation: We consider pressure-driven channel flow with constant mass flux. The x, y and z axes are aligned with the streamwise (overall flow), wall-normal and spanwise directions, respectively. Lengths are scaled by the half channel height l so the dimensionless channel height $L_y = 2$. The domain is periodic in x and z with periods L_x and L_z. Velocity $\boldsymbol{v}$ is scaled with the Newtonian laminar centerline velocity U; time t with l/U, and pressure p with ρU^2, where ρ is the fluid density. The polymer stress tensor $\boldsymbol{\tau}_p$ is related to the polymer conformation tensor $\boldsymbol{\alpha}$ through the FENE-P constitutive relation.

Here $Re = \rho U l / (\eta_s + \eta_p)$, where η_s and η_p are the solvent and polymer contributions to the zero-shear rate viscosity. The viscosity ratio $\beta = \eta_s / (\eta_s + \eta_p)$; polymer concentration is proportional to $1 - \beta$. We fix $\beta = 0.97$ and maximum extensibility $b = 6400$. The Weissenberg number
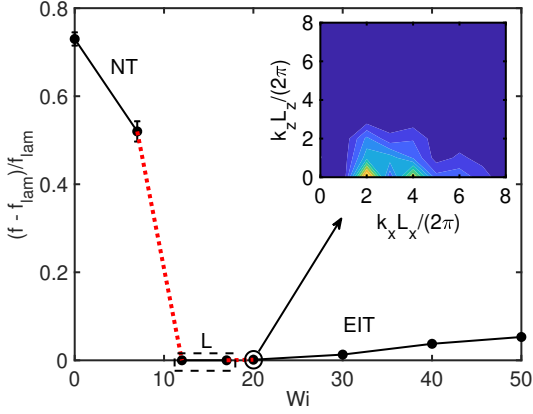
Figure 1: Scaled friction factor vs. Wi at $Re = 1500$. Abbreviations 'NT', 'L' and 'EIT' stand for Newtonian-like turbulence, laminar and elastoinertial turbulence, respectively. In most cases, the error bars are smaller than the symbols. Red dotted lines indicate the intervals of Wi in which the NT solution loses existence and the EIT solution comes into existence, respectively, as Wi increases. Inset shows the spatial spectrum of the wall normal velocity at $y = 0$ for $Wi = 20$. Here, x- and z-wavenumbers k_x and k_z are reported in scaled form, as $k_x L_x/2\pi$ and $k_z L_z/2\pi$. For inset, low is blue, high is yellow. Reproduced with permission from Shekar *et al.* (2019).

$Wi = \lambda U/l$, where λ is the polymer relaxation time, measures the ratio between the relaxation time for the polymer and the shear time scale for the flow.

For the nonlinear direct numerical simulations (DNS) described below, a finite difference scheme and a fractional time step method are adopted for integrating the Navier-Stokes equation. Second-order Adams-Bashforth and Crank-Nicolson methods are used for convection and diffusion terms, respectively. The FENE-P equation is discretized using a high resolution central difference scheme (Kurganov & Tadmor, 2000; Vaithianathan *et al.*, 2006; Dallas *et al.*, 2010). No artificial diffusion is applied. For the three-dimensional (3D) simulations, $(L_x, L_y, L_z) = (10, 2, 5)$; these were chosen to match Samanta *et al.* (2013). Typical resolution for the 3D runs at EIT is $(N_x, N_y, N_z) = (189, 150, 189)$. For the 2D runs at $Re = 3000$, $N_y = 302$ is used. For the linear analyses, the governing equations are linearized around the laminar solution and Fourier-transformed in x z, and t, are discretized in y with a Chebyshev pseudospectral method. Typically, about 200 Chebyshev polynomials are sufficient for the resolvent calculations, whereas as many as 400 are required for the TS eigenmode. The norm used in the resolvent calculations is consistent with the non-Euclidean geometry of positive-definite tensors (Hameduddin *et al.*, 2019).

Nonlinear simulation results: Fig. 1 illustrates 3D DNS results for scaled friction factor $(f - f_{lam})/f_{lam}$ vs. Weissenberg number Wi at $Re = 1500$. Here, f_{lam} is the value in laminar flow. At low but increasing Wi, the flow is turbulent, with f decreasing, indicating that the drag is reduced from the Newtonian value. In this regime, which we denote NT, the turbulence displays a streamwise vortex structure typical of Newtonian turbulence. With a further
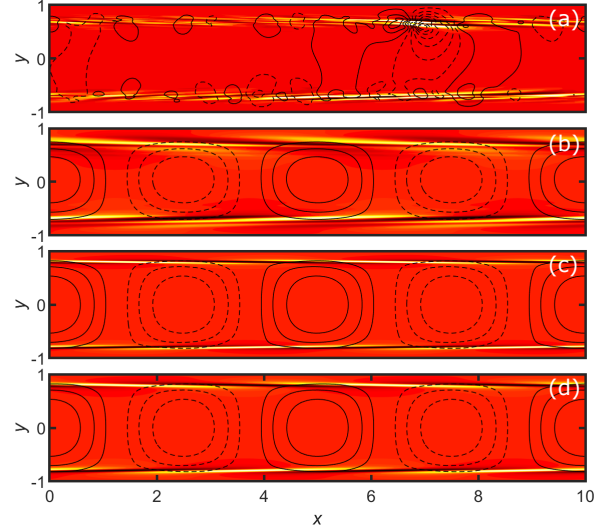

Figure 2: (a) Snapshot of v' (line contours) and α'_{xx} (filled contours) from 3D nonlinear DNS at $Re = 1500$, $Wi = 20$, where $'$ denotes fluctuations away from the mean profile. (b) Phase-matched average $(k_x L_x/2\pi, k_z L_z/2\pi) = (2, 0)$ structures from 3D DNS. (c) Structure of the TS mode at $Re = 1500, Wi = 20$, and the same wavenumbers as in (b). (d) Structure of the most strongly amplified resolvent mode at $Re = 1500, Wi = 20$, the same wavenumbers as in (b), and $c = 0.37$. In all plots, contour levels are symmetric about zero. For v' dashed - negative, solid - positive. For α'_{xx} black - negative, red - zero and yellow - positive. Reproduced with permission from Shekar *et al.* (2019).

increase in Wi, however, $f - f_{lam}$ drops to zero – the flow relaminarizes, as the NT regime loses existence. (At this Re and all Wi considered here, the laminar state is linearly stable.) At still higher Wi, the flow, if seeded with a sufficiently energetic initial condition, becomes turbulent again, with a very low value of $f - f_{lam}$ (consistent with experimental observations of Choueiri *et al.* (2018) in pipe flow) and a very different structure: i.e. a new kind of turbulence comes into existence. In this regime the flow structure corresponds to EIT as described by Samanta *et al.* (2013) and Sid *et al.* (2018); we further analyze this structure below.

We now focus on the flow structure in the EIT regime. The inset in Fig. 1 shows a spatial spectrum of the wall normal velocity at $y = 0$ (the channel centerplane), i.e., $|v(k_x, 0, k_z)|$. The centerplane is chosen because it yields the cleanest spectra. In the EIT regime, there is very strong spectral content when $k_z = 0$, indicating the importance of 2D mechanisms in the dynamics. Indeed, Sid *et al.* (2018) reports that EIT can arise in 2D simulations. Figure 2a shows a slice at $z = 2.5$ of the fluctuating wall normal velocity, v', and fluctuating xx-component of the polymer conformation tensor, α'_{xx}. Observe that α'_{xx} is strongly localized near $y = \pm 0.7 - 0.8$. While tilted sheets of polymer stretch fluctuations have already been noted as characteristic of EIT (Samanta *et al.*, 2013), the strong localization has not been previously observed, perhaps because prior results have been at higher Re and Wi, i.e. further from the point at which EIT comes into existence. Fig. 2b shows the dominant $(k_x L_x/2\pi, k_z L_z/2\pi) = (2, 0)$ component of the $Wi = 20$
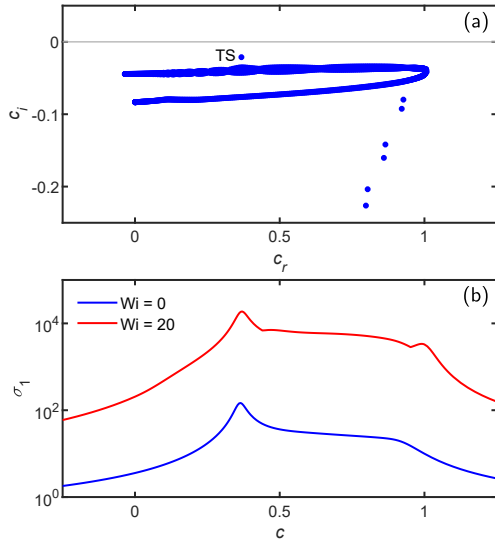
Figure 3: Eigenvalue spectrum for $(k_x L_x/2\pi, k_z L_z/2\pi) = (2,0)$ with $Wi = 20$ and $Re = 1500$. The eigenvalue labeled 'TS' corresponds to the TS mode. (b) Leading singular value of the resolvent operator for $Wi = 0$ and $Wi = 20$, plotted on a logarithmic scale. Reproduced with permission from Shekar *et al.* (2019).

results, phase-matched and averaged over many snapshots. Results for higher k_x are very similar, exhibiting strong localization of stress fluctuations in the same narrow bands.

Linear analyses: To shed light on the origin of the highly localized large stress fluctuations, we now consider the evolution of infinitesimal perturbations to the laminar state with given wavenumbers k_x, k_z. Two approaches are used. The first is classical linear stability analysis, in which solutions of the form $\hat{\phi}(x,y,z,t) = \phi(y)\exp[i(k_x x + k_z z - k_x ct)]$ are sought, resulting in an eigenvalue problem for the complex wavespeed c. The ^ indicates deviation from the laminar state – for the linear analyses described here, ^ and ′ are synonymous. If all $c_i < 0$, the flow is linearly stable. The second approach is to determine the linear response of the laminar flow to external forcing with given frequency ω using the resolvent operator (frequency-space transfer function) of the linearized equations (Schmid, 2007; McKeon & Sharma, 2010). In both analyses, the concept of *critical layers*, i.e., wall-normal positions where the fluid velocity equals the wavespeed of an eigenmode or resolvent mode, is important. While some recent studies suggest the importance of critical-layer mechanisms in viscoelastic shear flows (Page & Zaki, 2015; Lee & Zaki, 2017; Haward *et al.*, 2018; Hameduddin *et al.*, 2019), they do not make as direct a connection to EIT as we illustrate here.

Figure 3a shows the result of linear stability analysis (the eigenvalues c) for $Wi = 20$, $k_x L_x/2\pi = 2$, $k_z = 0$, the wavenumber corresponding to the dominant structures observed in the nonlinear simulations. All eigenvalues have $c_i < 0$ – the laminar flow is linearly stable.

Of note is the mode labeled 'TS', the viscoelastic continuation of the classical Tollmien-Schlichting mode (Drazin & Reid, 2004). Viscoelasticity has only a weak effect on the TS eigenvalue, which changes from $c = 0.362 -$

$0.019i$ to $c = 0.368 - 0.022i$ between $Wi = 0$ and $Wi = 20$ (Zhang *et al.*, 2013). Despite the small change in c, the conformation tensor disturbance depends very strongly on Wi; the peak value of α'_{xx} grows from zero at $Wi = 0$ to about 10^5 times the peak value of u' at $Wi = 20$.

The structure of this eigenmode is shown for $Wi = 20$ in Fig. 2c. In the Newtonian case, the disturbance velocity field is a train of spanwise-oriented vortices that span the entire channel; this structure is only weakly modified even at high Wi. The polymer stress disturbance behaves very differently: at $Wi = 20$ it consists of highly inclined sheets that are extremely localized around the critical layers $y = \pm 0.79$ for the TS wavespeed of $c_r \approx 0.37$. Comparison with Figs. 2a and 2b shows a strong similarity between the eigenmode and the tilted sheetlike structures that are the hallmark of EIT, with the resemblance between the TS mode and the $(k_x L_x/2\pi, k_z L_z/2\pi) = (2,0)$ structure from the DNS in Fig. 2b being particularly striking. Specifically, note that for the TS mode, Fig. 2c, v' and α'_{xx} are even and odd, respectively, with respect to $y = 0$, while in Fig. 2b and the corresponding results at higher wavenumbers, these symmetries hold to a good approximation.

Despite the fact that the TS mode ultimately decays, short-time disturbance growth or amplification of harmonic-in-time disturbances significant enough to trigger nonlinear effects is still possible (Schmid, 2007). We quantify this amplification by computing the largest singular value σ_1 of the resolvent operator. Figure 3b shows results for $Wi = 0$ and $Wi = 20$ in the same range of (real) wavespeeds $c = \omega/k_x$ depicted in Figure 3a. The amplification increases dramatically with Wi, with the values at $Wi = 20$ being $\sim 10^2$ times those for $Wi = 0$; this is consistent with the drastic increase in the conformation tensor disturbance amplitude already discussed for the TS mode. In both cases, the maximum amplification occurs for $c \approx 0.37$, which coincides with the wavespeed for the TS mode, indicating that the amplification is primarily normal in character, i.e., the large resolvent norm is primarily due to the close proximity of the TS eigenvalue to the real axis. The most-amplified disturbance is therefore expected to be closely linked to the TS wave. Figure 2d, which shows that the leading resolvent mode is almost identical to the TS eigenmode in Figure 2c, confirms that this is indeed the case. This result provides additional strong evidence that the structures observed in EIT are closely related to those in viscoelasticity-modified TS waves.

Self-sustained viscoelastic Tollmien-Schlichting waves: The strong peak in the EIT spectrum seen in Figure 1 corresponds to a wavelength of 5, so here we report computations of self-sustained nonlinear TS waves in a 2D domain with this length. In Newtonian flow, the solution family exists at this wavelength down to $Re \approx 2800$ and the upper branch solution is linearly stable and thus easily computed via DNS (Jiménez, 1990; Mellibovsky & Meseguer, 2015; Herbert, 1979). We continue the Newtonian solution at $Re = 3000$ to the parameters of interest ($\beta = 0.97$ and $b = 6400$) at $Wi = 0.1$, then increase Wi to study the effect of viscoelasticity. Hameduddin *et al.* (2019) have also computed nonlinear viscoelastic TS waves in the regime $Re > 5772$ and noted the role the critical layer plays in polymer stretching at high Wi, but have not reported the observations described below.

On increasing Wi, the self-sustained nonlinear viscoelastic TS wave at $Re = 3000$ develops sheets of high

polymer stretch resembling near wall structures seen at EIT. This structure originates in the nonlinear Kelvin cat's eye kinematics of TS waves at finite amplitude, as detailed in Shekar *et al.* (2019). At the parameters chosen, the solution branch originating in the self-sustained Newtonian TS wave bifurcates to a periodic orbit at $Wi \approx 3.5$ (cf. Lee & Zaki (2017)) before turning back into a traveling wave and losing existence beyond $Wi = 3.875$. While we cannot show this definitively, the likely bifurcation scenario is that the solution branch turns around in a saddle-node bifurcation, yielding a lower branch TS wave solution that becomes the Newtonian solution as $Wi \to 0$. This scenario is shown on Fig. 4.

Fig. 4(a) also shows the EIT solution branch, which loses existence at finite amplitude when $Wi \lesssim 13$. The bifurcation underlying this transition is presumably also of saddle-node form. Using EIT at $Wi = 13$ as an initial condition for a run at $Wi = 12$, EIT persists transiently for hundreds of time units before eventually decaying, not to the laminar state, but to a very weak nontrivial flow, which we henceforth call the "lower branch attractor" (LBA). We elaborate on this attractor below. Figure 5a shows the evolution of the mean wall shear rate during the decay process. The mean wall shear rate displays a substantial drop between $t = 200$ and $t = 500$ during which the top half of the channel decays away. Figure 5b is a snapshot at $t = 200$, just before this drop. Strong striations of polymer stretch typical of EIT make up this structure. At later times, the bottom half of the channel sustains the dynamics for a few hundred time units. Figure 5c is a snapshot at $t = 1000$ during this "quasi-EIT" phase. Strong striations can be clearly seen in the bottom half which remain absent from the top half during this phase. There is no special preference to either half of the channel and for other starting initial conditions, the bottom can be seen to decay first.

As time increases further, the structure continues to decay, as shown in Fig. 5d at $t = 1540$, but does not ultimately reach the laminar state. Instead, as shown in Fig. 5e at $t = 2000$, it evolves to a state with very weak stress fluctuations localized around $y \approx \pm 0.82$, which we call the "lower branch attractor" (LBA). This state, while weakly chaotic, strongly resembles the linear TS mode at these parameters, as we now further illustrate.

Lower branch attractor: To elaborate on the relationshship between the LBA and the linear TS mode, we now describe 2D simulation results at $Re = 3000, Wi = 13, L_x = 5$, i.e. close to the point where the 2D EIT branch first comes into existence as shown in the bifurcation diagram (Figure 4). Figure 6 shows the evolution of the L_2-norm of $\hat{\alpha}_{xx}$ starting from an initial condition consisting of the laminar state plus some amplitude ε of the linear TS mode for this parameter set. Here, ^ denotes fluctuations from the laminar state. For weak perturbations ($\varepsilon = 1$, which corresponds to magnitudes shown in figure 7a), the expected decay to the laminar state is observed (the laminar state is linearly stable). However, for larger perturbations where nonlinear mechanisms start to play a role, the solution evolves to the LBA. For comparison, the dashed line shows the linearized evolution starting from the same initial conditions, which decays to laminar, thus highlighting the role of nonlinearity in the transition to the LBA. This state is robust: initial perturbation amplitudes over a wide range will evolve to it, as shown in Figure 6. Initial conditions with very large magnitudes ($\varepsilon = 6000$) evolve to EIT: both EIT and LBA are
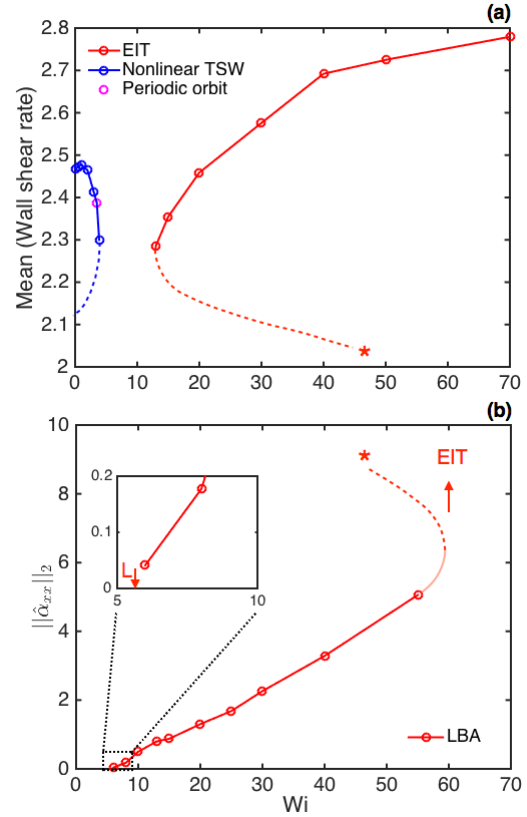

Figure 4: (a) Bifurcation diagram showing the evolution of the mean wall shear rate with Wi for the 2D nonlinear TSW and EIT branches at $Re = 3000, L_x = 5$. (b) Bifurcation diagram of the L_2-norm of $\hat{\alpha}_{xx}$ with Wi for the LBA. Light red corresponds to the hypothesized part of the LBA, indicating loss of existence between $Wi = 55$ and 60. Dashed curves are hypothesized unstable solution branches that are consistent with the DNS data and principles of bifurcation theory. The asterisks on the plots indicate that the continuation of the branch from one plot to the other.

stable states at the chosen parameters.

Resolution tests were performed to ensure satisfactory convergence of statistics for the LBA. A resolution of $(N_x, N_y) = (79, 302)$ is used for the following results.

Figure 7a shows the linear TS mode structure at these parameters. Figure 7b is a snapshot showing the typical fluctuation structure of the LBA. The bulk structure of the LBA has sheets of $\hat{\alpha}_{xx}$ highly localized near $y = \pm 0.82$ and wall normal velocity contours across the entire channel. This bears strong resemblance to the TS mode shown in figure 7a, which also displays a critical layer structure localized at $y = \pm 0.82$. The LBA is thus a weakly nonlinear self-sustaining state whose primary structure is the viscoelastic TS mode. In this state, the velocity fluctuations are very weak, and the mean wall shear rate displays a negligible change from laminar. This can be understood on the grounds that changes of the mean wall shear rate correspond to fluctuations with $k_x = 0$, which arise only due to nonlinear interactions. Since the primary structure is very weak, the nonlinear effects will be even weaker.

To briefly illustrate nonlinear effects, Figures 7c and 7d, respectively, show the $k_x L_x / 2\pi = 1, 2$, Fourier compo-

Figure 6: L_2-norm of $\hat{\alpha}_{xx}$ for $Re = 3000, Wi = 13, L_x = 5$, starting from an initial condition of laminar state + $\varepsilon \times$ TS-mode. Dashed lines correspond to linearized runs starting from the same initial conditions for $\varepsilon = 10$ and 100.
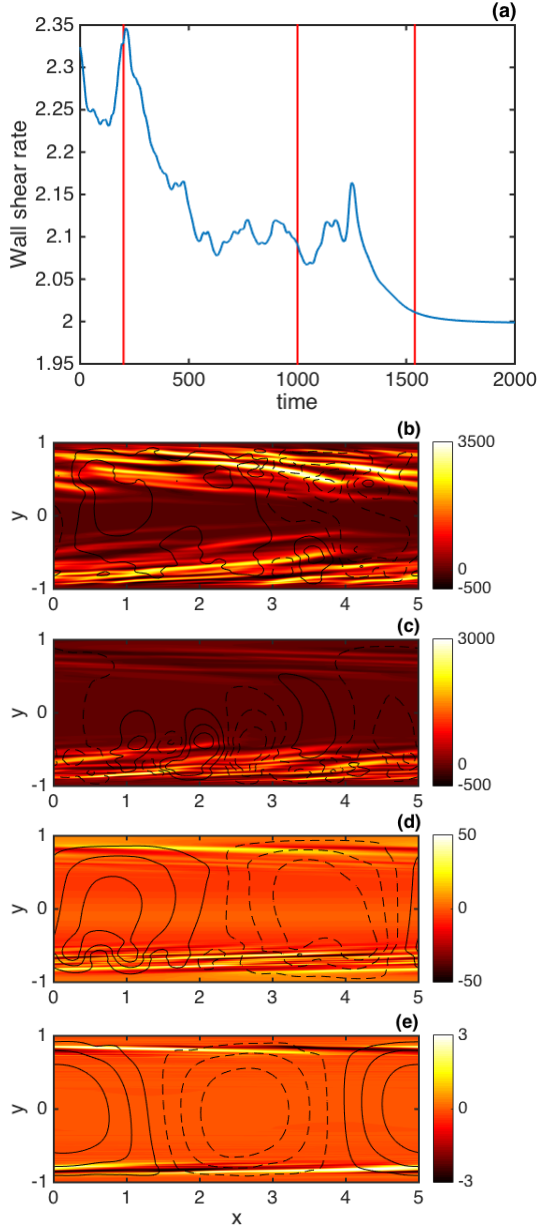

Figure 5: (a) Wall shear rate vs time for $Re = 3000, Wi = 12$ starting from initial condition at EIT at $Wi = 13$. (b), (c), (d), (e) snapshots at instants indicated by the red lines at t = 200, 1000, 1540 and 2000 respectively. Shown are contour lines of wall normal velocity $\hat{v}$ superimposed on color contours of $\hat{\alpha}_{xx}$ where ˆdenotes deviations from the laminar state. For $\hat{v}$, dashed = negative and solid = positive.

nents of the snapshot shown in 7b. It is clear to see from Figure 7c the resemblance to the TS mode. At $k_x L_x/2\pi = 2$ polymer fluctuations localized near the wall in the region $y = \pm 0.6 - 0.8$ can be observed in Figure 7d, with this observation holding as well for higher wavenumbers. Unlike the TS mode, these higher wavenumber modes may instantaneously generate velocity fields primarily localized to one half of the channel.

Having established the structure of the flow on the LBA branch, we now illustrate the bifurcation scenario of this solution branch by continuing in Wi. The LBA branch loses
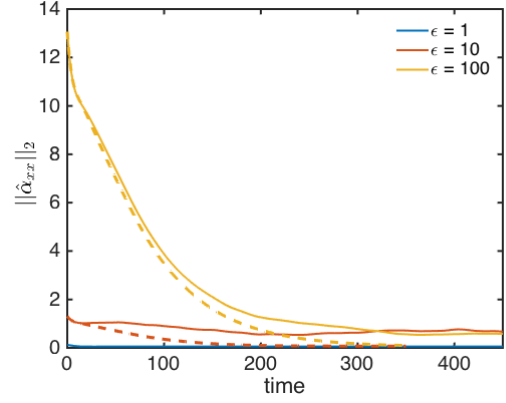
existence at finite amplitude (i.e. in a saddle-node bifurcation) for $Wi \lesssim 6$, as we have confirmed both by using the $Wi = 6$ solution as an initial conditions for simulations at lower Wi and by running simulations starting from the laminar state at a given Wi perturbed by the TS mode with small ε. For $Wi < 6$ all these initial conditions decay to laminar. On increasing Wi, the LBA loses existence between $Wi = 55$ and $Wi = 60$, again presumably in a saddle-node bifurcation, and initial conditions that land on the LBA for $Wi = 55$ evolve to EIT. These observations suggest that the LBA turns around and forms an unstable branch that joins up with the unstable lower branch of EIT. Due to the small amplitude of the LBA branch, the bifurcation scenario associated with it is shown separately in Figure 4b, using the L_2 norm of $\hat{\alpha}_{xx}$ as the amplitude measure. The unresolved regime between $Wi = 55$ and $Wi = 60$ where the LBA loses existence is shown in light red. The hypothesized unstable branch connecting LBA and EIT is shown schematically with dashed lines on the bifurcation diagrams and the asterisks indicate how they are connected in moving from Figure 4a to Figure 4b.

Conclusions

Elastoinertial turbulence at low Re has strongly localized stress fluctuations, suggesting the importance of critical-layer mechanisms in its origin. These fluctuations strongly resemble the most slowly decaying structures from linear stability analysis, as well as the most strongly amplified disturbances as determined by resolvent analysis of the linearized equations. Finally, using as an initial condition the laminar state plus a small amplitude Tollmien-Schlichting perturbation, we find a stable small-amplitude self-sustaining nonlinear state, the "lower branch attractor". This state has structure that very closely resembles the viscoelastic TS mode. and appears to be directly connected to EIT in parameter space. Taken together, these results suggest that, at least in the parameter range considered here, the bypass transition leading to EIT is mediated by nonlinear amplification and self-sustenance of perturbations that generate TS-wave-like flow structures.
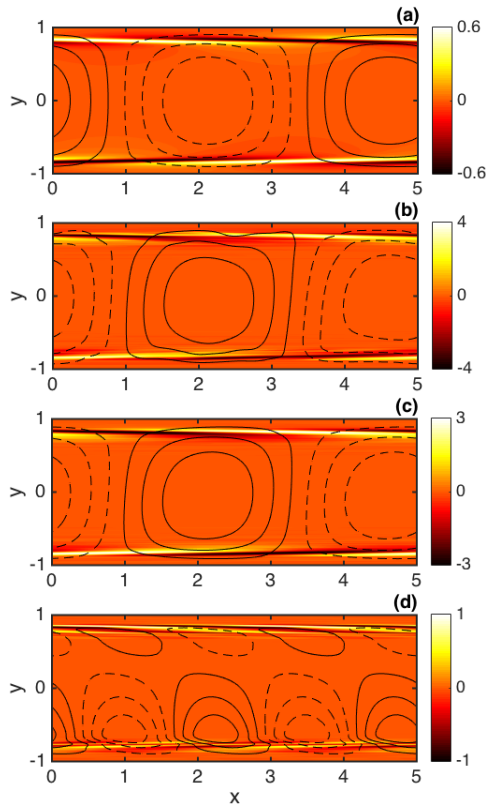
Figure 7: (a) Structure of the TS mode at $Re = 3000, Wi = 13, L_x = 5$. Magnitude of the eigenmode is arbitrary and values shown here correspond to $\varepsilon = 1$ perturbation. (b) Snapshot of the fluctuation structure of the LBA at $Re = 3000, Wi = 13$. (c) and (d) are the $k_x L_x/2\pi = 1, 2$ components respectively, of the snapshot shown in (b). Shown are contour lines of $\hat{v}$ superimposed on color contours of $\hat{\alpha}_{xx}$. For $\hat{v}$, dashed = negative and solid = positive.

REFERENCES

Chandra, B., Shankar, V. & Das, D. 2018 Onset of transition in the flow of polymer solutions through microtubes. *J. Fluid Mech.* **844**, 1052–1083.

Choueiri, G. H., Lopez, J. M. & Hof, B. 2018 Exceeding the Asymptotic Limit of Polymer Drag Reduction. *Phys. Rev. Lett.* **120** (12), 124501.

Dallas, V., Vassilicos, J. & Hewitt, G. 2010 Strong polymer-turbulence interactions in viscoelastic turbulent channel flow. *Phys. Rev. E* **82** (6), 066303.

Drazin, P. G. & Reid, W. H. 2004 *Hydrodynamic Stability*, 2nd edn. *Cambridge Mathematical Libraries* . Cambridge University Press.

Dubief, Y., Terrapon, V. E. & Soria, J. 2013 On the mechanism of elasto-inertial turbulence. *Phys. Fluids* **25** (11), 110817.

Forame, P. C., Hansen, R. J. & Little, R. C. 1972 Observations of early turbulence in the pipe flow of drag reducing polymer solutions. *AIChE Journal* **18** (1), 213–217.

Garg, P., Chaudhary, I., Khalid, M., Shankar, V. & Subramanian, G. 2018 Viscoelastic pipe flow is linearly unstable. *Phys. Rev. Lett.* **121** (2), 024502.

Hameduddin, I., Gayme, D. F. & Zaki, T. A. 2019 Perturbative expansions of the conformation tensor in viscoelastic flows. *J. Fluid Mech.* **858**, 377–406.

Haward, S. J., Page, J., Zaki, T. A. & Shen, A. Q. 2018 Inertioelastic Poiseuille flow over a wavy surface. *Phys. Rev. Fluids* **3** (9), 091302.

Herbert, T. 1979 Periodic secondary motions in a plane channel. In *Proceedings of the Fifth International Conference on Numerical Methods in Fluid Dynamics June 28–July 2, 1976 Twente University, Enschede*, pp. 235–240. Springer.

Hoyt, J. W. 1977 Laminar-turbulent transition in polymer solutions. *Nature* **270**, 508–509.

Jiménez, J. 1990 Transition to turbulence in two-dimensional Poiseuille flow. *J. Fluid Mech.* **218**, 265–297.

Kurganov, A. & Tadmor, E. 2000 New high-resolution central schemes for nonlinear conservation laws and convection–diffusion equations. *J. Comput. Phys.* **160** (1), 241–282.

Lee, S. J. & Zaki, T. A. 2017 Simulations of natural transition in viscoelastic channel flow. *J. Fluid Mech.* **820**, 232–262.

McKeon, B. J. & Sharma, A. S. 2010 A critical-layer framework for turbulent pipe flow. *J. Fluid Mech.* **658**, 336–382.

Mellibovsky, F. & Meseguer, A. 2015 A mechanism for streamwise localisation of nonlinear waves in shear flows. *J. Fluid Mech.* **779**, R1.

Page, J. & Zaki, T. A. 2015 The dynamics of spanwise vorticity perturbations in homogeneous viscoelastic shear flow. *J. Fluid Mech.* **777**, 327–363.

Samanta, D., Dubief, Y., Holzner, M., Schäfer, C., Morozov, A. N., Wagner, C. & Hof, B. 2013 Elasto-inertial turbulence. *Proc. Nat. Acad. Sci.* **110** (26), 10557–10562.

Schmid, P. J. 2007 Nonmodal stability theory. *Annu. Rev. Fluid Mech.* **39**, 129–162.

Shekar, A., McMullen, R. M., Wang, S. N., McKeon, B. J. & Graham, M. D. 2019 Critical-Layer Structures and Mechanisms in Elastoinertial Turbulence. *Phys. Rev. Lett.* **122** (12), 124503.

Sid, S., Terrapon, V. E. & Dubief, Y. 2018 Two-dimensional dynamics of elasto-inertial turbulence and its role in polymer drag reduction. *Phys. Rev. Fluids* **3** (1), 011301.

Vaithianathan, T., Robert, A., Brasseur, J. G. & Collins, L. R. 2006 An improved algorithm for simulating three-dimensional, viscoelastic turbulence. *J. Non-Newtonian Fluid Mech.* **140** (1-3), 3–22.

Virk, P. S., Mickley, H. S. & Smith, K. A. 1970 The ultimate asymptote and mean flow structure in Toms' phenomenon. *J. Appl. Mech.* **37** (2), 488–493.

Zhang, M., Lashgari, I., Zaki, T. A. & Brandt, L. 2013 Linear stability analysis of channel flow of viscoelastic Oldroyd-B and FENE-P fluids. *J. Fluid Mech.* **737**, 249–279.